

Electronic, optical, and thermoelectric properties of Janus In-based monochalcogenides

Tuan V Vu^{1,2} , Vo T T Vi³, Huynh V Phuc⁴, Chuong V Nguyen⁵ ,
N A Poklonski⁶ , C A Duque⁷ , D P Rai⁸ , Bui D Hoi³  and
Nguyen N Hieu^{9,10,*} 

¹ Division of Computational Physics, Institute for Computational Science, Ton Duc Thang University, Ho Chi Minh City 700000, Vietnam

² Faculty of Electrical & Electronics Engineering, Ton Duc Thang University, Ho Chi Minh City 700000, Vietnam

³ Department of Physics, University of Education, Hue University, Hue 530000, Vietnam

⁴ Division of Theoretical Physics, Dong Thap University, Cao Lanh 870000, Vietnam

⁵ Department of Materials Science and Engineering, Le Quy Don Technical University, Ha Noi 100000, Vietnam

⁶ Department of Physics, Belarusian State University, Minsk 220030, Belarus

⁷ Instituto de Física, Universidad de Antioquia UdeA, Calle 70 No. 52-21, Medellín, Colombia

⁸ Physical Sciences Research Center (PSRC), Department of Physics, Pachhunga University College, Mizoram University, Aizawl 796001, India

⁹ Institute of Research and Development, Duy Tan University, Da Nang 550000, Vietnam

¹⁰ Faculty of Natural Sciences, Duy Tan University, Da Nang 550000, Vietnam

E-mail: vuvantuan@tdtu.edu.vn and hieunn@duytan.edu.vn

Received 28 December 2020, revised 6 March 2021

Accepted for publication 30 March 2021

Published 4 May 2021



Abstract

Inspired by the successfully experimental synthesis of Janus structures recently, we systematically study the electronic, optical, and electronic transport properties of Janus monolayers In_2XY ($X/Y = \text{S, Se, Te}$ with $X \neq Y$) in the presence of a biaxial strain and electric field using density functional theory. Monolayers In_2XY are dynamically and thermally stable at room temperature. At equilibrium, both In_2STe and In_2SeTe are direct semiconductors while In_2SSe exhibits an indirect semiconducting behavior. The strain significantly alters the electronic structure of In_2XY and their photocatalytic activity. Besides, the indirect–direct gap transitions can be found due to applied strain. The effect of the electric field on optical properties of In_2XY is negligible. Meanwhile, the optical absorbance intensity of the Janus In_2XY monolayers is remarkably increased by compressive strain. Also, In_2XY monolayers exhibit very low lattice thermal conductivities resulting in a high figure of merit ZT , which makes them potential candidates for room-temperature thermoelectric materials.

Keywords: Janus group-III monochalcogenides, electronic structure, photocatalytic activity, low-thermal conductivity, first-principles calculations

(Some figures may appear in colour only in the online journal)

* Author to whom correspondence should be addressed.

1. Introduction

Since its successful exploration, graphene has created a great revolution in the study of two-dimensional (2D) nanomaterials [1]. With outstanding physical and chemical properties, graphene has been widely applied in electronic and optoelectronic devices [2–4]. In parallel with the study of graphene, an extensive search for 2D graphene-like materials took place. Many 2D layered structures have been explored and joined the 2D family, including silicene [5], germanene [6], transition metal dichalcogenides (TMDs) [7], and monochalcogenides [8]. Besides, a series of theoretical studies on this material family has been performed by using different approaches [9–15]. Among them, monolayers of the group III monochalcogenides, which have been experimentally synthesized [16–19], emerged as nanomaterials with great prospect for applications in high-performance water-splitting and optoelectronic devices [20, 21]. Recent studies have shown that 2D materials exhibit extremely low lattice thermal conductivity and they can be used as thermoelectric materials even though their figure of merit is less than one [22, 23].

Recently, a new type of 2D layered-materials, Janus structure of TMDs, has been experimentally synthesized [24, 25]. By replacing a layer of chalcogen atom with another layer of chalcogen atom, one can obtain the Janus structure from TMDs. However, this replacement has led to a remarkable change in the geometric structure of TMDs, which is closely related to their physical properties. The Janus MoSSe with the vertical asymmetric structure has experimentally been released [24]. The loss of mirror symmetry in the Janus structure has led to novel physical properties, which were not found in the originals of MoS₂ or MoSe₂ [26, 27]. It is found that the electron states of the Janus TMDs can be modulated by a strain engineering [28] or electric field [29]. Also, the absorbance of the monolayer MoSeTe is up to $1.0 \times 10^6 \text{ cm}^{-1}$ which is perfect for applications in optoelectronics [30]. Also, the Janus TMDs have suitable band alignments for photocatalytic applications [31].

Motivated by the success of the Janus TMDs, some theoretical studies have recently been done on Janus structures of monochalcogenides [32, 33]. Guo and co-workers have found that the Janus monolayers based group-III monochalcogenides possess semiconducting behavior with energy gap depending strongly on chalcogen elements [34]. Kandemir and Sahin have also indicated that strain engineering is one of the best ways to change the electronic structure of the Janus monolayers [35]. Using density functional theory (DFT) study, it is confirmed that the Janus group-III monochalcogenide monolayers have a broad absorption spectrum, extending from the visible light region to the near-ultraviolet one [32]. Using the Boltzmann transport function, Wan's group revealed that the thermal conductivity of the Janus monolayers of group III monochalcogenides can be altered by the size of the sample and their heat transport depend greatly on the long-range harmonic and anharmonic interactions, which exists in most 2D monochalcogenides [33].

In this study, we present systematically our DFT calculations for the electronic, photocatalytic, optical, and electronic

transport properties of In₂XY ($X/Y = \text{S, Se, Te}; X \neq Y$) monolayers under a biaxial strain and electric field. Via the consideration of the phonon spectra and *ab initio* molecular dynamics (AIMD) simulations, we first analyze the stabilities of monolayers. To obtain the most accurate band gap, different functionals were used to calculate the band structure. From the investigation of band edge alignment, the photocatalytic characteristics of the Janus structures were concluded. The basic thermoelectric properties have also been studied based on the semi-classical Boltzmann transport equation. We focus comprehensively on the influence of the biaxial strain and electric field on these physical properties of the Janus monolayers with a wide range of both strain and electric field. Our findings not only show the potential application in next-generation optoelectronic devices of the Janus monolayers In₂XY, but also motivate experimental studies of this material family in the future.

2. Computational details

We perform the calculations in this work within the framework of DFT with projector-augmented wave pseudopotentials as implemented in the quantum espresso code [36]. The generalized gradient approximations (GGA) of Perdew–Burke–Ernzerhof (PBE) [37] were used to consider the exchange–correlation interaction and the spin–orbit coupling (SOC) was included in self-consistent calculations for electron states [38]. The cut-off energy for the plane-wave basis is set to be 500 eV. In the Brillouin zone (BZ), a $(15 \times 15 \times 1)$ k -mesh is sampled for calculations. All investigated structures, including the cell parameters and positions of atoms, were fully optimized. The criteria for the energy convergence between steps and the force during relaxation were 10^{-6} eV and 10^{-3} eV Å⁻¹, respectively. To break unphysical interactions between periodic images of systems, a vacuum space of 20 Å in the vertical direction (along z -axis) is applied. Also, to most accurately obtain the band gap of In₂XY monolayers, the hybrid functional by Heyd–Scuseria–Ernzerhof (HSE06) [39] was used in our calculations.

For the phonon spectrum calculations, we constructed a large supercell of $4 \times 4 \times 1$ to obtain the more accurate results. To confirm the thermal stability of the systems, we use the AIMD simulations [40], which are performed via the Nose-thermostat algorithm at room temperature for 6 ps with 6000 time steps. A $(30 \times 30 \times 1)$ k -mesh is used for investigations of the optical properties. In this work, the GGA-PBE method is used to investigate the thermoelectric properties of monolayers. To obtain accurate transport coefficients, in the first Brillouin zone, a $90 \times 90 \times 1$ k -point mesh is used. The electronic transport coefficients of the Janus In₂XY monolayers are calculated via the semi-classical Boltzmann transport theory within the constant scattering time and rigid band approximations as performed in the BoltzTrap [41]. The calculations for the lattice thermal conductivity is performed by using the Phono3py package [42]. The lattice thermal conductivity is obtained by solving the linearized Boltzmann equation from first-principles anharmonic lattice dynamics calculations within an iterative self-consistent method. The constant

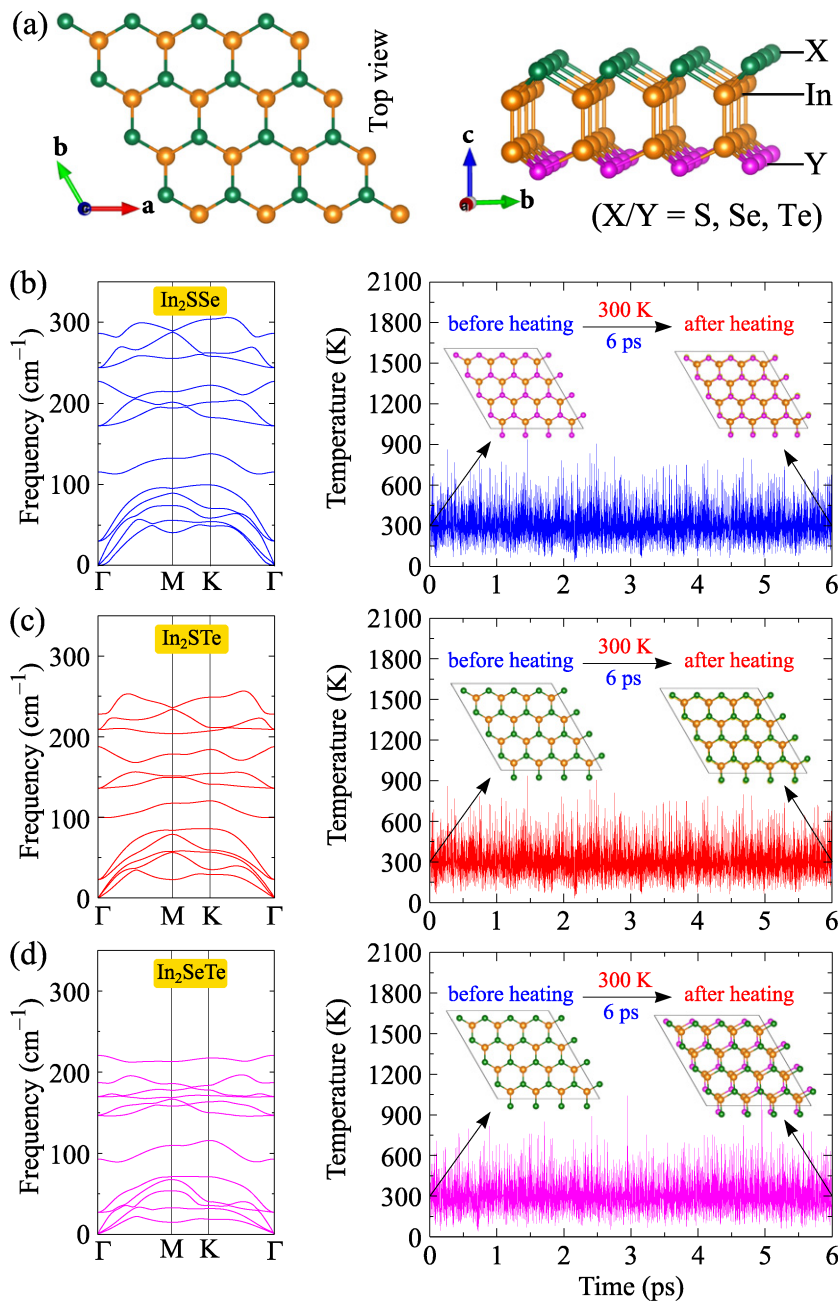


Figure 1. (a) Views of atomic structure of Janus monolayers In_2XY ($X/Y = \text{S, Se, Te}$; $X \neq Y$). Phonon spectra and AIMD simulations of temperature fluctuation as a function of time at 300 K of In_2SSe (b), In_2STe (c), and In_2SeTe (d).

temperature canonical ensemble is used in our calculations for the electronic transport properties.

3. Structure and stability

The group III monochalcogenide monolayers have layered structure with hexagonal lattice [20] and we can construct the Janus group III monochalcogenide structures from these monochalcogenides. For instance, the Janus structures In_2XY can be constructed from InX monolayers. By replacement the bottom layer X atoms by Y atoms in InX monolayer, one can form three possible Janus structures In_2SSe , In_2STe , and In_2SeTe . The optimized crystal structures of the Janus In_2XY monolayer is displayed in figure 1(a). Compared to

monochalcogenides, Janus structures In_2XY have been broken the mirror symmetry and inversion symmetry. The Janus structures In_2XY belong to the $P3m1$ (C_{3v}) group symmetry. The geometric symmetry in 2D nanomaterials is an important characteristic that determines their electronic and transport properties. Within each Janus structure, there is a significant difference between In-X and In-Y bond lengths. For instance, the In-Se and In-Te bond lengths in Janus In_2SeTe are 2.709 Å and 2.854 Å, respectively. The In-X bond length $d_{\text{In-X}}$ and also the X-In-In bond angle $\phi_{\angle\text{XInIn}}$ increase as the X atom varies from S to Te, which is strongly connected with the atomic radius of X element. However, the In-In bond lengths in all three Janus structures are nearly equal, about 2.830 Å.

Table 1. The obtained calculations for lattice constants a (Å), bond lengths d (Å), thicknesses Δ (Å), the S–In–In bond angle $\phi_{\angle \text{SInIn}}$ (deg), the Se–In–In bond angle $\phi_{\angle \text{SeInIn}}$ (deg), and the Te–In–In bond angle $\phi_{\angle \text{TeInIn}}$ (deg) of Janus In_2SSe , In_2STe , and In_2SeTe .

	a	$d_{\text{In-In}}$	$d_{\text{In-S}}$	$d_{\text{In-Se}}$	$d_{\text{In-Te}}$	Δ	$\phi_{\angle \text{SInIn}}$	$\phi_{\angle \text{SeInIn}}$	$\phi_{\angle \text{TeGaGa}}$
In_2SSe	4.005	2.830	2.579	2.652	—	5.269	116.269	119.310	—
In_2STe	4.172	2.830	2.624	—	2.838	5.372	113.374	—	121.926
In_2SeTe	4.234	2.827	—	2.709	2.854	5.466	—	115.509	121.070

The in-plane lattice constants of In_2SSe , In_2STe , and In_2SeTe monolayers after optimization are 4.005 Å, 4.172 Å, and 4.234 Å, respectively. Our calculated results are consistent with the previous DFT studies [32, 33], in which the lattice constant of In_2SSe reported by Wan *et al* [33] and Huang *et al* were 4.005 Å and 4.015 Å, respectively. However, the lattice constant of In_2SSe reported Kandemir and Sahin [35] and da Silva [43] were respectively 3.88 Å and 3.84 Å, which is smaller than that achieved by the present work as well as by other groups [32, 33]. This difference can come from the selection and optimization of parameters during the computation, where the obtained results from DFT calculations strongly depend on the methodology, the level of accuracy, convergence criteria, and especially size of the supercell. There is very little information available on the parameters used for the computational procedure, especially size of the supercell, in the works by Kandemir and Sahin [35] and da Silva [43]. Kandemir and Sahin used a kinetic-energy cutoff of 400 eV and criteria for total force of 10^{-4} eV Å $^{-1}$, which are slightly different from the parameters used in our calculation. Unfortunately, to best of our knowledge, there are no experimental results on Janus In_2XY monolayers up to date. Our obtained results for structural parameters of Janus structures are summarized in table 1.

To test the dynamical stabilities, phonon dispersion relations of Janus structures In_2XY have been calculated through the whole Brillouin zone as presented in figure 1. The primitive cell of the Janus In_2XY monolayers contains four atoms (two In and two different chalcogen atoms). Therefore, the phonon spectrum of the In_2XY monolayers has 12 modes, including three acoustic modes and nine optical modes. There is no gap between the optical and acoustic modes. There is a frequency interval where both optical and acoustical modes coexist. This leads to strong acoustic-optical scattering and also increase the group velocity of phonon-phonon scattering, which plays an important role in reducing thermal conductivity. In the optical modes, there are three doubly degenerate at the Γ point and only three nondegenerate modes. The vibrational frequencies in In_2SeTe as shown in figure 1(d) are much smaller compared to those in other Janus structures as shown in figures 1(b) and (c). The phonon frequency, especially the frequency of the optical modes, depends strongly on the size of the chalcogen atoms. Maximum frequency of the optical branches decreases as the chalcogen atom changes from S to Te. Maximum frequency of the optical modes for In_2SSe , In_2STe , and In_2SeTe are around 305 cm $^{-1}$, 255 cm $^{-1}$, and 222 cm $^{-1}$, respectively. All three Janus structures In_2XY are confirmed to be dynamically stable because no negative frequencies are found in their

phonon spectra. It implies that the Janus structures In_2XY can be synthesized as freestanding monolayers.

The thermal stability of materials is a critical property to guarantee that they can be used in practical applications. In this work, the thermal stability of In_2XY is examined by AIMD simulations at 300 K for 6 ps (6000 time steps). Atomic structure snapshots before/after heating and the time-dependent temperature fluctuation of In_2XY by AIMD simulations are also displayed in figures 1(b)–(d). Obtained results confirm that the Janus In_2XY monolayers possess high thermal stability. The atomic structure of In_2XY is only slightly distortion and still robust after heating at 300 K by AIMD simulations. Besides, neither broken bond nor structural reconstruction takes place in In_2XY structures at 300 K.

4. Electronic properties

The electronic properties of In_2XY monolayers were calculated by using different approaches and obtained results for their band structures and partial density of states (PDOS) are presented in figure 2. It is found that the Janus structures In_2XY are semiconductors. While both In_2STe and In_2SeTe exhibit the direct semiconducting characteristics with the valence band maximum (VBM) and conduction band minimum (CBM) located at the Γ point, In_2SSe possesses an indirect gap with the VBM at the Γ -path. Our findings reveal that the Janus In_2SSe monolayer has the widest band gap. The obtained band gaps by the PBE method of In_2SSe , In_2STe , and In_2SeTe are 1.540 eV, 0.905 eV, and 1.075 eV, respectively. Our results are consistent with available data [34]. Focusing on the Janus In_2SSe , it is an indirect semiconductor with indirect band gap of $E_{\text{g}}^{\Gamma\text{M}\rightarrow\Gamma} = 1.541$ eV at the PBE level. The bands around the Γ point which are close to the VBM are quite flat. This may lead to producing a large amount of effective masses of the VBM, which has occurred in Janus SnSSe [44]. The difference between indirect $E_{\text{g}}^{\Gamma\text{M}\rightarrow\Gamma}$ and direct $E_{\text{g}}^{\Gamma\rightarrow\Gamma}$ gaps is extremely small (~ 0.05 eV). The calculated direct band gap of the In_2SSe using the PBE functional is $E_{\text{g}}^{\Gamma\rightarrow\Gamma} = 1.594$ eV. We know that the electronic properties of 2D monolayers are sensitive to their geometrically structural perfection. Therefore, a small difference in energy between direct and indirect band gaps can lead to the expectation that there will be indirect–direct gap transition when the Janus In_2SSe monolayer is under strain engineering or even electric field. Previously, Kandemir and Sahin have reported that the Janus In_2SSe monolayer is found to be a direct semiconductor [35]. This result is contradictory to our results as well as the results reported by Wan and co-workers [33]. The difference in band structure of

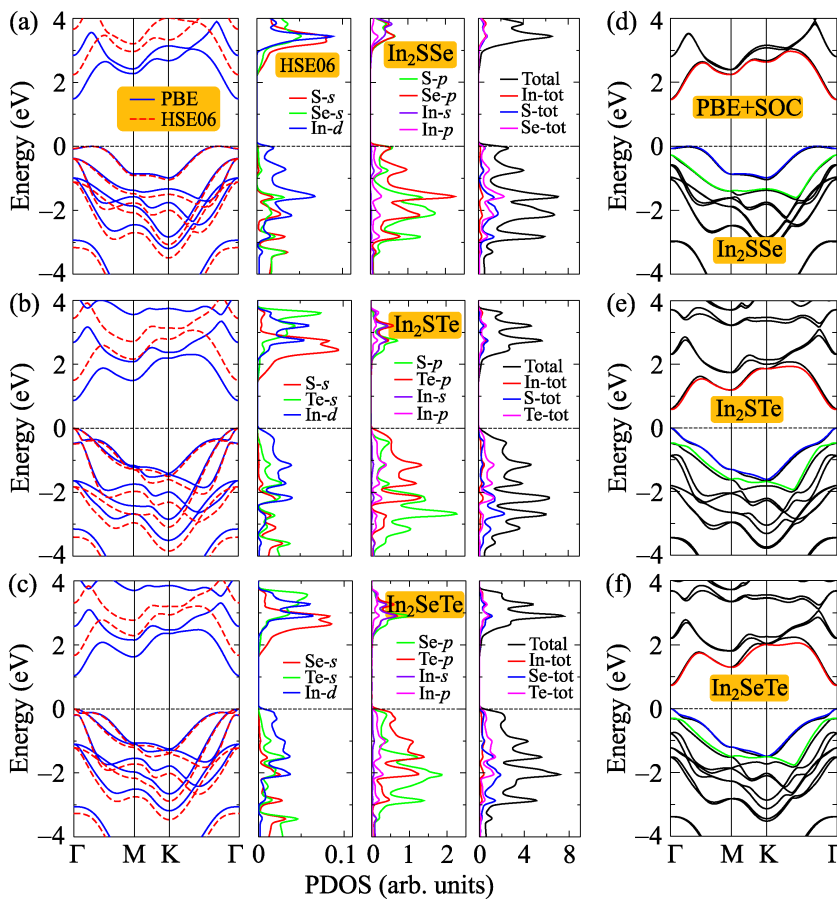


Figure 2. The calculated band structures of Janus In_2XY monolayers using the PBE and HSE06 (a)–(c) and PBE + SOC methods (d)–(f). Presented density of states in (a)–(c) are carried out by using the HSE06 functional. In (d)–(f), the blue and green lines have been used to highlight the splitting bands.

Table 2. Calculated band gaps (eV) using the PBE E_g^{PBE} , HSE06 E_g^{HSE06} , and PBE + SOC $E_g^{\text{PBE+SOC}}$ methods. The spin–orbit splitting value ΔE (eV) by PBE + SOC method.

	E_g^{PBE}	E_g^{HSE}	$E_g^{\text{PBE+SOC}}$	ΔE	Type	VBM \rightarrow CBM
In_2SSe	1.540	2.241	1.511	0.203	Indirect	$\Gamma\text{M} \rightarrow \Gamma$
In_2STe	0.905	1.495	0.682	0.476	Direct	$\Gamma \rightarrow \Gamma$
In_2SeTe	1.075	1.663	0.828	0.304	Direct	$\Gamma \rightarrow \Gamma$

In_2SSe between our results and those from Kandemir’s group is derived from the difference in lattice constants obtained from the two groups. The obtained result for the lattice constant of In_2SSe by Kandemir and Sahin is $a = 3.88 \text{ \AA}$ and the corresponding band structure has a direct band gap. However, when the In_2SSe under small biaxial strain, the obtained results by Kandemir and Sahin demonstrated that the Janus In_2SSe becomes an indirect semiconductor at the strain of +2% (the corresponding lattice parameter at the strain of 2% is 3.96 \AA) [35]. As above-mentioned, our result for the lattice constant of In_2SSe is 4.005 \AA , which is consistent with the previous results reported by Wan and co-workers with a lattice constant of 4.015 \AA and In_2SSe to be an indirect semiconductor [33]. The calculated results for band gap and related information of the Janus In_2XY monolayer are listed in table 2.

The SOC effects play a key factor in determining the electron states of the 2D systems, especially heavy metal-based compounds. In this study, effect of SOC on the band structures of the In_2XY has been examined. The obtained results for band structures of In_2XY using PBE + SOC approach are shown in figures 2(d)–(f). Due to the SOC effect, each energy band splits into two bands. The blue and green lines have been used to highlight the splitting bands in figures 2(d)–(f). It is seen that while the SOC effect slightly reduces the band gaps of the Janus monolayers In_2SSe and In_2STe , the band gap of In_2SeTe is reduced by up to 22.98% when the SOC is included, namely from $E_g^{\text{PBE}} = 1.075 \text{ eV}$ to $E_g^{\text{PBE+SOC}} = 0.828 \text{ eV}$. Besides, at the Γ -point, a spin–orbit splitting energy ΔE occurs in the valence band. Due to the Janus structure of heavy metals, high spin–orbit splitting values have been found in the Janus In_2XY

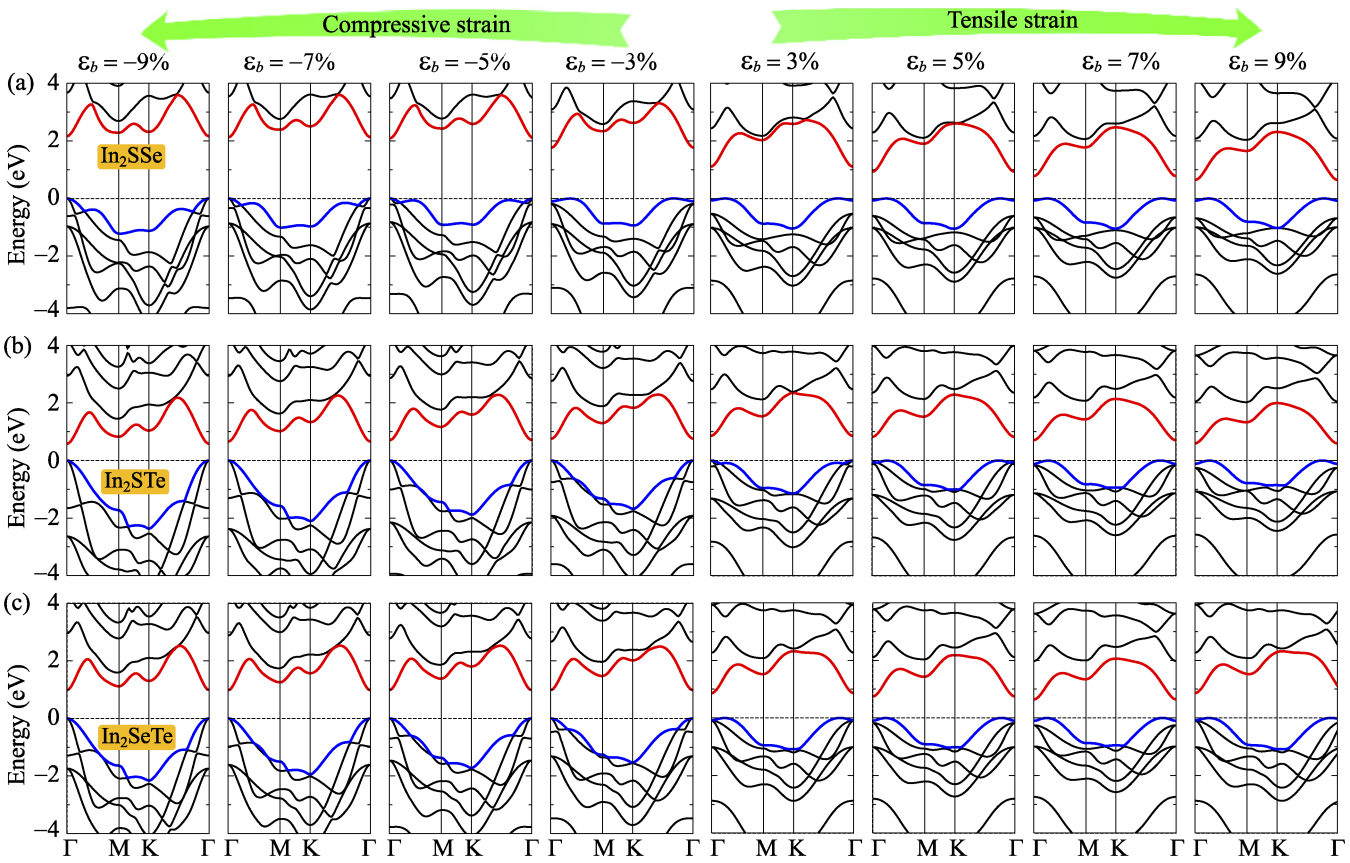


Figure 3. Band structures of the Janus monolayers (a) In_2SSe , (b) In_2STe , and (c) In_2SeTe under strain ε_b .

monolayer when the SOC effect is taken into account. Our findings demonstrate that the spin-orbit splitting value in the Janus In_2STe is largest, $\Delta E_{\text{In}_2\text{STe}} = 0.476$ eV. The spin-orbit splitting values in In_2SSe and In_2SeTe monolayer are respectively 0.203 eV and 0.304 eV. Previously, the high spin-orbit splitting values have been also found for Janus monolayers PtSSe (0.280 eV) [45] and SnSSe (0.266 eV) [44]. Also, spin splitting of the uppermost valence band in Janus dichalcogenide WSeTe monolayer up to 0.46 eV [46] and high valley spin splitting (0.449 eV) around the K point has been found in WSe monolayer due to the SOC effect [47].

It is well known that the PBE approach underestimates the energy gap of the semiconductors [48]. However, the band gap problem of nanomaterials can be solved through the use of hybrid functional [39] or GW approximation [49]. In the present work, the HSE06 functional [39] was also used to obtain most accurate energy gap of structures. The estimated band structures of In_2XY by the HSE06 functional are presented in figures 2(a)–(c). It is found that the band structures of Janus monolayers at the PBE and HSE06 levels have a similar profile. However, the calculated energy gaps by the HSE06 functional is higher than that by the PBE method. At the HSE06 level, the energy gaps of In_2SSe , In_2STe , and In_2SeTe monolayer are 2.241 eV, 1.495 eV, and 1.663 eV, respectively. Besides, to estimate the contribution of atomic orbitals to the electronic bands, the partial density of states (PDOS) of all three In_2XY structures were calculated using the HSE06 functional as presented in figures 2(a)–(c). It is

found that the valence bands of the Janus monolayers are greatly contributed from the p -orbitals of the chalcogen atoms. Also, the contribution of $\text{In}-d$ orbital to the conduction band is significant.

Physical properties of 2D nanomaterials, including monochalcogenides and Janus structures, are extremely sensitive to the perfection of structure. Strain engineering can strongly modulate their electronic properties. We next investigate the effect of a biaxial strain on the electronic properties of In_2XY monolayers. For a quantitative estimate, we introduce the biaxial strain ε_b defined by $\varepsilon_b = (a - a_0)/a_0$. Here, a_0 and a are respectively the lattice parameters of monolayers before and after strain. In this work, a large range of ε_b from -10% to 10% is applied to In_2XY monolayers. Band structures of In_2XY monolayers under different levels of ε_b are shown in figure 3. Our calculated results reveal that the strain engineering may be the cause of the indirect-direct gap transition in In_2XY . As presented in figure 3(a), it is found that the band structures, especially the valence bands, of the Janus structures are strongly altered by strain ε_b . Under a compressive strain $\varepsilon_b < 0$, in the Janus In_2SSe monolayer as presented in figure 3(a), the VBM locating on the $\Gamma\text{-M}$ -path tends to shift to the Γ point and the Janus In_2SSe monolayer becomes a direct semiconductor under a compressive strain from -7% to -10% . Meanwhile, direct-indirect gap transitions were also found in In_2STe and In_2SeTe monolayers at certain values of tensile strain as depicted in figures 3(b) and (c). The CBM in the In_2STe and In_2SeTe remains at the

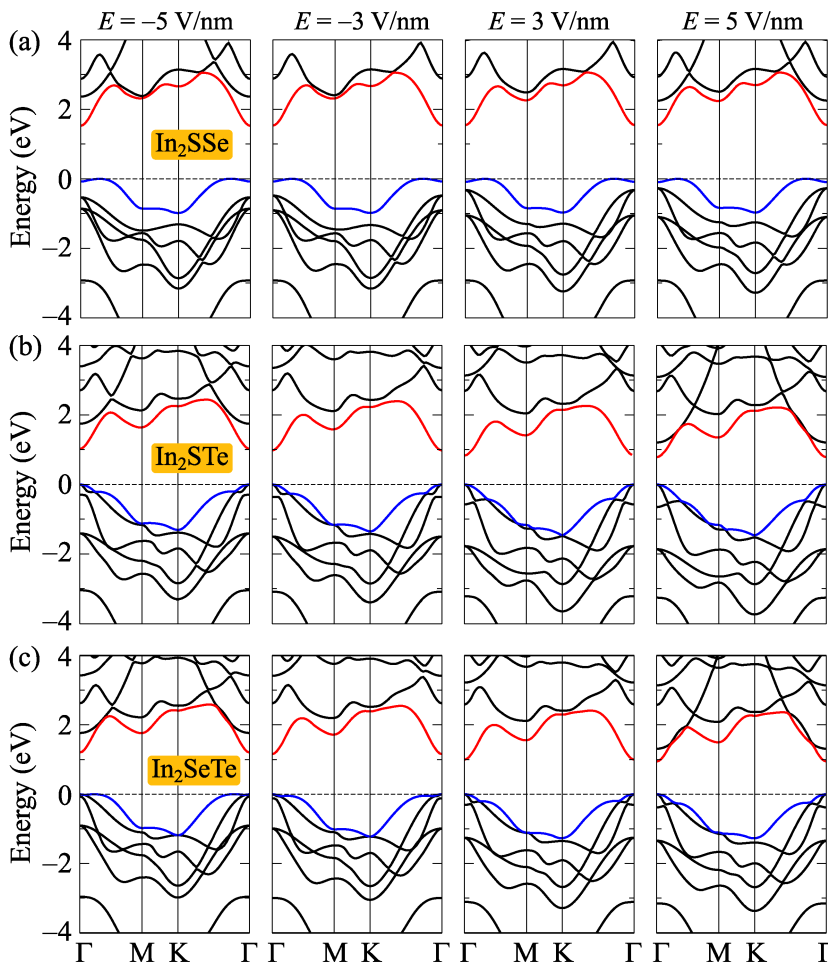


Figure 4. Band structures of the Janus In_2XY monolayers under an electric field E : (a) In_2SSe , (b) In_2STe , and (c) In_2SeTe .

Γ -point, while the tensile strain can cause it to move from the Γ -point to ΓM -path. The direct-indirect gap transitions occur at $\varepsilon_b = 5\%$ and $\varepsilon_b = 3\%$ in In_2STe and In_2SeTe monolayers, respectively.

Contrary to the strain cases, the effect of the electric field E on the electron states of the Janus In_2XY monolayers is quite weak. In our study, an external electric field E with strengths from 0 to $\pm 5 \text{ V nm}^{-1}$ is applied to the Janus structures perpendicularly (along the c -axis). Our calculations for band structures of the Janus In_2XY monolayers under an external electric field E are presented in figure 4. Obtained results indicate that there is no phase transition in In_2SSe and In_2STe when E was applied as presented in figures 4(a) and (b). However, as shown in figure 4(c), the VBM in the In_2SeTe tends to leave the Γ -point and move out the middle of the ΓM -path when the negative E was applied. As a result, the Janus In_2SeTe becomes an indirect semiconductor at $E = -5 \text{ V nm}^{-1}$ with the CBM locating at the Γ -point and the VBM on the ΓM -path. Also, while the effect of strain on the energy gaps of the Janus structures is remarkable, the dependence of their band gap on the E is quite weak. The variation of the band gap as a function of the ε_b and E is illustrated in figure 5. From figure 5(a) we can conclude that the band gap of the Janus In_2SeTe monolayer is almost independent of the compressive strain while the compressive strain slightly reduces the band gap of the Janus

In_2STe monolayer, from 0.905 eV at equilibrium ($\varepsilon_b = 0$) to 0.702 eV at $\varepsilon_b = -10\%$. However, there is a big difference in the Janus In_2SSe monolayer case. The band gap of In_2SSe was greatly increased (and reached a maximum value of 2.386 eV at $\varepsilon_b = -9\%$) in the presence of compressive strain. Besides, the band gaps of both In_2SSe and In_2SeTe decrease gradually in the case of $\varepsilon_b > 0$. In the $\varepsilon_b > 0$ case, the energy gap of the In_2SeTe increases slightly and then decreases. At $\varepsilon_b = 10\%$, the difference in band gap between the Janus structures is very small, about 0.1 eV. Focusing the effect of the electric field E on the band gaps as shown in figure 5(b). The band gaps depend linearly on E . In the electric field range from -5 V nm^{-1} to 5 V nm^{-1} , while the band gap of In_2SSe is almost unchanged, the band gaps of both In_2STe and In_2SeTe decrease, but the reduction is quite small, for example band gap of In_2STe (In_2SeTe) at $E = -5 \text{ V nm}^{-1}$ is 1.022 eV (1.203 eV) compared to 0.784 eV (0.943 eV) at $E = 5 \text{ V nm}^{-1}$. With a large direct gap that can be controlled by external conditions, the Janus structures In_2XY could have potential applications in optoelectronics.

The band gap connects strongly to the ability to apply materials in photocatalytic applications. The redox potential of water splitting, which can be evaluated via the conduction/valence band edges, depended on the pH value [50]. The standard reduction potential for H^+/H_2 is given by

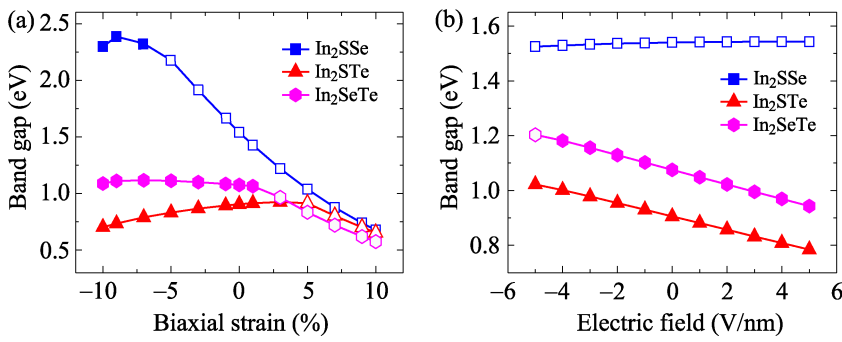


Figure 5. The variation of the band gap of the Janus In₂XY monolayers as functions of the biaxial strain ε_b (a) and electric field E (b). Filled and empty symbols refer to the direct and indirect band gaps, respectively.

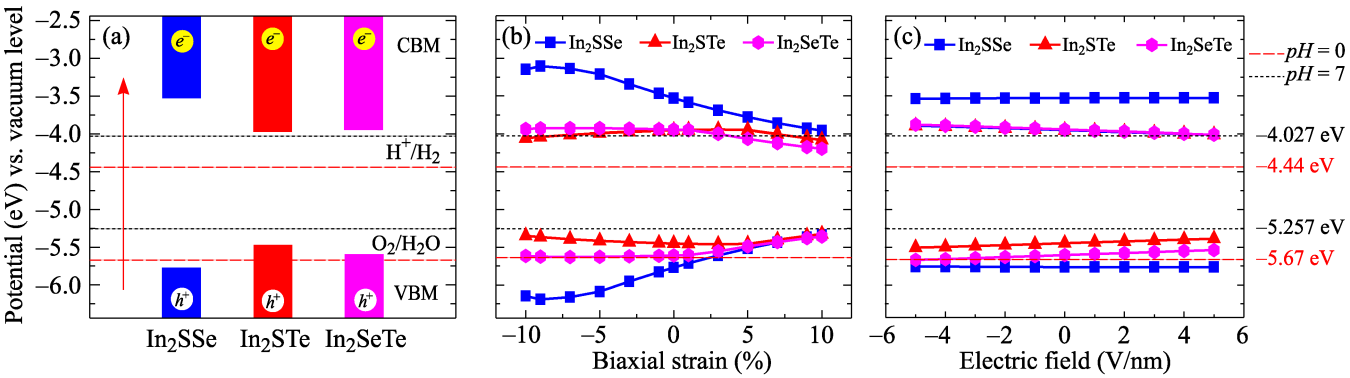


Figure 6. Band edge alignments of Janus In₂XY monolayers at equilibrium (a) and under different levels of biaxial strain (b) and electric field (c). The calculated potential is reference to the vacuum level. The horizontal dashed and dotted lines refer, respectively, to the redox standard potentials for water splitting at pH = 0 and pH = 7 for reference.

$E_{H^+/H_2} = -4.44 + 0.059 \times \text{pH}$ and the standard oxidation potential for O₂/H₂O is $E_{O_2/H_2O} = -5.67 + 0.059 \times \text{pH}$ [51]. At pH = 0, the standard redox potentials are $E_{H^+/H_2} = -4.44$ eV and $E_{O_2/H_2O} = -5.67$ eV reference to the vacuum level or $E_{H^+/H_2} = 0$ eV and $E_{O_2/H_2O} = 1.23$ eV reference to the normal hydrogen electrode (NHE). Therefore, the required band gap for photocatalysts must be larger than 1.23 eV. It implies that all three Janus structures In₂XY, which have the band gaps larger than 1.23 eV at the HSE06 level as listed in table 2, have potential for water splitting photocatalysts. However, the band alignments of all structures should be evaluated and compare with the redox potentials of water to confirm their photocatalytic activity. The conduction band E_{CBM} and valence band E_{VBM} edge potentials can be calculated by using the Mulliken electronegativity χ and band gap value E_g , which are given by [52]

$$E_{VBM} = \chi - E_{elec} + \frac{1}{2}E_g, \quad (1)$$

$$E_{CBM} = E_{VBM} - E_g, \quad (2)$$

where E_{elec} is the free electron energy. In this part, the band gaps of the Janus structures are calculated by using the HSE06 functional.

The evaluations for the band edge positions E_{CBM} and E_{VBM} of the Janus structures In₂XY are presented in figure 6(a). Our findings demonstrate that, at pH = 0, only the Janus In₂SSe monolayer can serve as a photocatalyst for water

splitting with suitable band edge positions of $E_{CBM} = -3.529$ eV and $E_{VBM} = -5.770$ eV. The Janus In₂STe and In₂SeTe monolayers do not possess photocatalytic activity for water splitting at pH = 0 because their E_{VBM} is higher than the standard oxidation potential for O₂/H₂O meaning that the VBM is not enough to activate the hydrogen evolution. In the case of pH = 7, standard redox potentials reference to the vacuum level are $E_{H^+/H_2} = -4.027$ eV and $E_{O_2/H_2O} = -5.257$ eV. As presented in figure 6, all Janus structures In₂XY have suitable band edge alignments for water splitting, especially the In₂STe and In₂SeTe because they have direct-gaps. In the presence of the ε_b , as depicted in figure 6(b), we can see that the bias potentials in the Janus In₂STe and In₂SeTe monolayers are reduced by strain. However, the photocatalytic activity of the Janus In₂SSe monolayer can be enhanced by the compressive strain. Effect of the electric field, as shown in figure 6(c), on the band edge positions of all three Janus structures is small and does not significantly change their photocatalytic properties.

5. Optical properties

The fundamental optical properties can be expressed via their frequency-dependent dielectric constant defined as $\varepsilon(\omega) = \varepsilon_1(\omega) + i\varepsilon_2(\omega)$. In principle, $\varepsilon_2(\omega)$ is usually estimated first, then using the Kramers–Kronig relation we can obtain the real part $\varepsilon_1(\omega)$. The $\varepsilon_2(\omega)$ can be obtained by summing of the

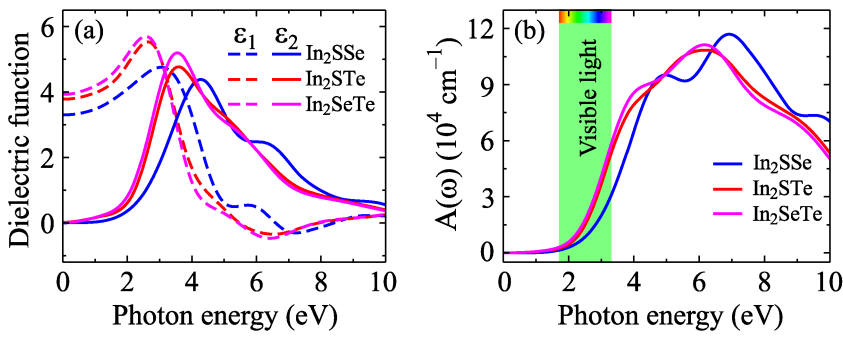


Figure 7. The calculated dielectric functions (a) and absorption coefficient ε_b (b) of the Janus In_2XY monolayer at equilibrium.

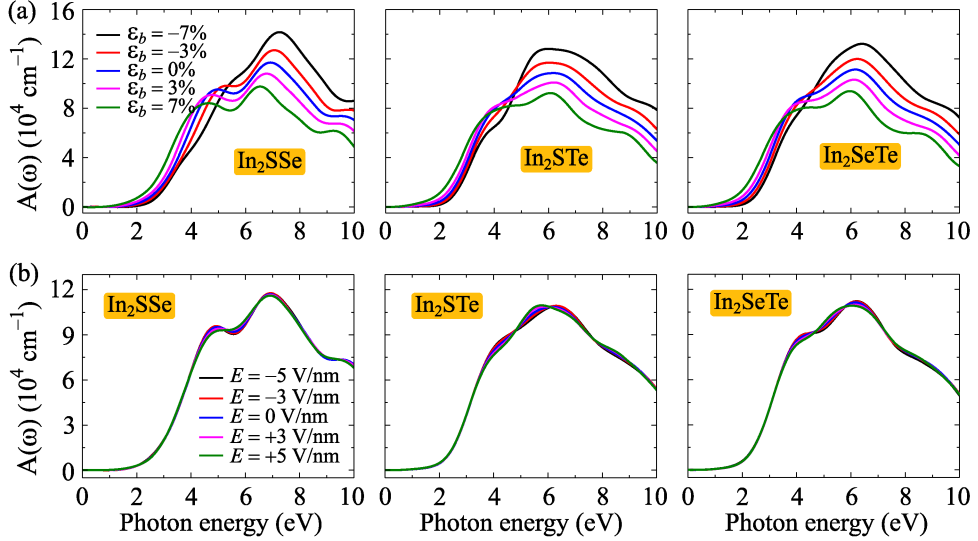


Figure 8. Calculated absorption spectra of the Janus In_2XY monolayers under the strain (a) and electric field (b) effects.

filled–empty state transitions [53, 54]:

$$\varepsilon_2(\omega) = \frac{4\pi^2 e^2}{Vm^2 \omega^2} \sum_{nn'\sigma} \langle kn\sigma | p_i | kn'\sigma \rangle \langle kn'\sigma | p_j | kn\sigma \rangle \times f_{kn}(1 - f_{kn'}) \delta(E_{kn'} - E_{kn} - \hbar\omega), \quad (3)$$

where e/m is the charge/mass of an electron, V is the volume of the unit-cell, p is the momentum operator, $|kn\rangle$ is the crystal wave-function, and f_{kn} is the Fermi distribution function.

The absorption coefficient $A(\omega)$ is given by [55]:

$$A(\omega) = \frac{\sqrt{2}\omega}{c} \left[\sqrt{\varepsilon_1(\omega)^2 + \varepsilon_2(\omega)^2} - \varepsilon_1(\omega) \right]^{1/2}. \quad (4)$$

In figure 7, we present the obtained results for the dielectric function and absorption coefficient $A(\omega)$ of the In_2XY at equilibrium. As depicted in figure 7(a), we can see that the static dielectric constant $\varepsilon_1(0)$ of In_2SeTe is the highest. However, the static dielectric constant is not much larger than that of the In_2STe monolayer. The static dielectric constants of the Janus In_2SSe , In_2STe , and In_2SeTe monolayer are respectively 3.301, 3.793, and 3.931. Our obtained results are consistent with the previous DFT calculations [32]. The main peaks in $\varepsilon_2(\omega)$ spectrum of the Janus In_2XY monolayers are located at the incoming photon energy around 4 eV which are caused by

the interband transition. The main peak in $\varepsilon_2(\omega)$ of the In_2SSe monolayer lies in a higher energy region compared to those of In_2STe and In_2SeTe monolayers. This is consistent with their band gaps. As illustrated in figure 7(b), the absorption coefficient $A(\omega)$ of the Janus In_2XY monolayers is activated in the visible light region because they own the narrow band gaps. The intensity of $A(\omega)$ rapidly increases in the visible-light region to its maximum value in the near-ultraviolet one. The absorption spectra of the In_2STe and In_2SeTe monolayers are almost the same with main peaks at about 6 eV. In the range from 0 to 10 eV of the incident light energy, there are two peaks in $A(\omega)$ of In_2SSe . The main peak is on the higher incoming photon energy side, at 7 eV with an intensity of $11.705 \times 10^4 \text{ cm}^{-1}$. The intensity of the main peak in the absorption spectrum of the Janus In_2SSe monolayer is higher than those of both Janus In_2STe and In_2SeTe monolayers. However, in the visible light region, the $A(\omega)$ of the In_2SSe ($3 \times 10^4 \text{ cm}^{-1}$ at 3.3 eV) is smaller than that in the In_2STe and In_2SeTe monolayers ($5.5 \times 10^4 \text{ cm}^{-1}$).

The absorption spectra $A(\omega)$ of In_2XY monolayers under the biaxial strain ε_b and electric field E are depicted in figure 8. It is found that while the influence of E on $A(\omega)$ is negligible as presented in figure 8(b), the $A(\omega)$ depends greatly on ε_b (see figure 8(a)). In the presence of the tensile strain $\varepsilon_b > 0$, the

absorption intensity of Janus structures In_2XY is reduced and the absorption peaks move to a lower energy region. Meanwhile, their absorption intensity can be enhanced significantly by compressive strain in the near-ultraviolet region. Besides, the compressive strain has caused the absorption peaks to shift to a higher energy region. Especially the first lower peak in the absorption spectrum of the In_2SSe monolayer tends to disappear under the compression strain. At $\varepsilon_b = -7\%$, there is only one peak in the absorption spectrum of the In_2SSe monolayer with very high absorption intensity up to $14.172 \times 10^4 \text{ cm}^{-1}$.

6. Thermoelectric properties

Since 1993, low-dimensional nanomaterials have been predicted to be potential thermal materials [56]. The thermoelectric conversion efficiency of materials can be estimated by the figure of merit [57]

$$ZT = S^2 \sigma T \frac{1}{\kappa_e + \kappa_l}, \quad (5)$$

where S is the Seebeck coefficient, σ is the electrical conductivity, T is the temperature, and κ_e and κ_l are respectively the electronic and lattice components of the thermal conductivity.

One of the key factors of the thermoelectric properties of thermal materials is the relaxation time τ . The relaxation time is estimated through the carrier mobility μ as $\tau = m^* \mu / e$ [58, 59] with m^* being the effective mass. The carrier mobility μ is calculated by using the Bardeen and Shockley's deformation potential theory [60, 61]. The relaxation time depends mostly on scatterings. In this study, the electron scattering is included in our calculations. Also, previous work has indicated that the carrier mobility of 2D nanomaterials depends weakly on the carrier density [62]. Hence, we propose that the τ does not depend on the doping level N . This assumption is consistent with previous DFT calculations, that there is no significant difference between the relaxation time in the n -type and p -type cases of MoS_2 monolayer [63]. The assumption for the doping level-independent relaxation time has also been used previously to calculate the electronic transport properties of the Janus structures [44, 64]. Our calculated results reveal that at 300 K, In_2SSe has the longest electron relaxation time of $6.020 \times 10^{-15} \text{ s}$, while the relaxation time of In_2STe and In_2SeTe is $2.882 \times 10^{-15} \text{ s}$ and $1.039 \times 10^{-15} \text{ s}$, respectively. In a previous study, the relaxation time τ is fitted as $5.17 \times 10^{-14} \text{ s}$ for MoS_2 monolayer at room temperature [59]. The temperature-dependence of the relaxation time is depicted in figure 9. The relaxation time decreases gradually with temperature. In the higher temperature region, the smaller the difference in the relaxation time between the Janus structures.

By using the semi-classical Boltzmann transport theory within the rigid band approximation, we calculate the transport coefficients, such as the Seebeck coefficient S , electrical conductivity σ , and power factor $S^2\sigma$ at room temperature of 300 K of the Janus In_2XY monolayers by the PBE method. In figure 9, we plot the doping level dependence of the S , σ , and $S^2\sigma$ of the Janus In_2XY monolayers at room temperature. Coefficients S and σ are related to the band structure and density of

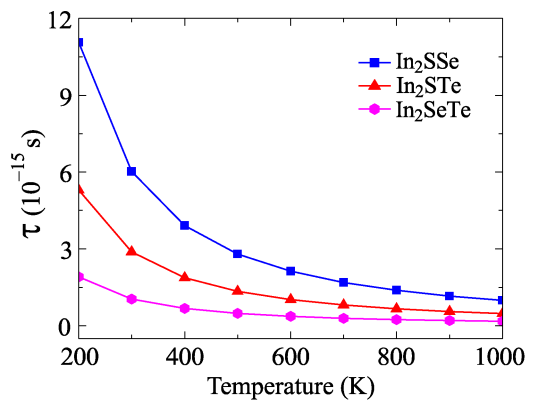


Figure 9. Temperature dependent relaxation time τ of the Janus In_2XY monolayers.

states near the Fermi energy. The flat band gives the high hole mass while sharp band gives lower hole mass in the k -space. Doping of heavy elements modifies the energy bands near the Fermi energy thus improves the Seebeck as well as electrical conductivity. Also, the doping of heavy element reduced the lattice thermal conductivity as the doped element of heavier masses act like a barrier to enhance the rate of phonon scattering. Previously, the dependence of thermoelectric properties on the carrier concentration of SnS crystal has been experimentally measured [65]. In the low-dimensional systems, instead of using doping concentration, the doping level N , which refers to the carrier number per unit cell, was used [45]. The negative and positive values of N stand for the n - and p -type doping, respectively. Our calculated results, as shown in figure 10(a), demonstrate that the Seebeck coefficients of In_2XY monolayers are very close in the case of n -type doping. The p -type S in the In_2SSe monolayer is higher than that in both In_2STe and In_2SeTe monolayer as presented in figure 10(a). The differences in σ between the monolayers are also evident in the case of n -type doping as depicted in figure 10(b). We focus on the power factor $S^2\sigma$ in the N range from -0.02 to 0.02 as illustrated in figure 10(c). In general, the power factor for p -doping is higher than that for n -doping.

As presented in equation (5), the thermal conductivity, including electronic κ_e and lattice κ_l thermal conductivity, play an important role in determining the value of the figure of merit ZT . In figure 11(a), we present our calculations for dependence of the electronic thermal conductivity κ_e on the doping level N at 300 K. The κ_e of monolayers has a similar doping level N dependent with the electrical conductivity, in which the value of κ_e of In_2SSe in the n -type is much greater than in the p -type. The lattice thermal conductivity κ_l has a great contribution to thermal conductivity. We assume that κ_l does not depend on the doping level. We have calculated the lattice thermal conductivity κ_l using Phono3py package [42]. Our obtained results indicate that the Janus structures In_2XY has very low lattice thermal conductivity. At room temperature, In_2STe has the highest κ_l of 0.324 W mK^{-1} . Meanwhile, the lattice thermal conductivity at 300 K of In_2SSe and In_2SeTe is only 0.109 W mK^{-1} and 0.011 W mK^{-1} , respectively. The κ_l of In_2XY monolayers is close to that of TlInTe_2 (0.370 W mK^{-1}) [66] but much smaller than that of

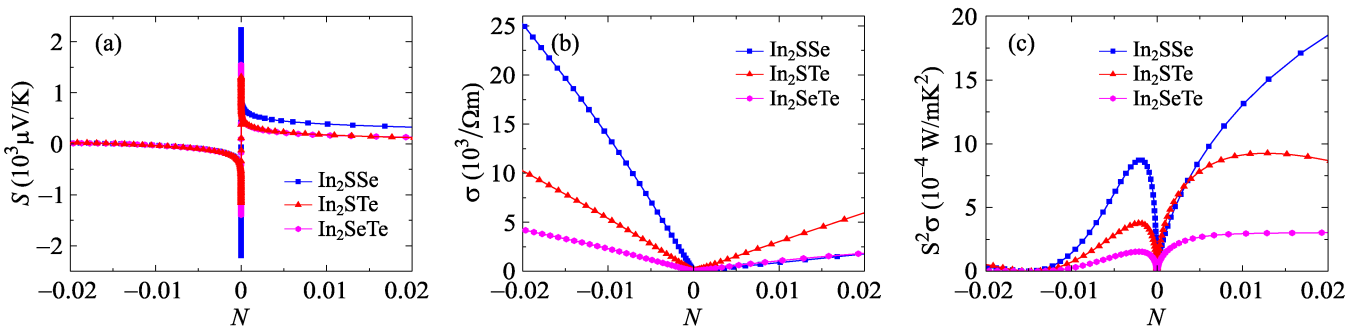


Figure 10. (a) Seebeck coefficient S , (b) electrical conductivity σ , and (c) power factor $S^2\sigma$ as a function of the doping level N at room temperature in the Janus In_2XY monolayers.

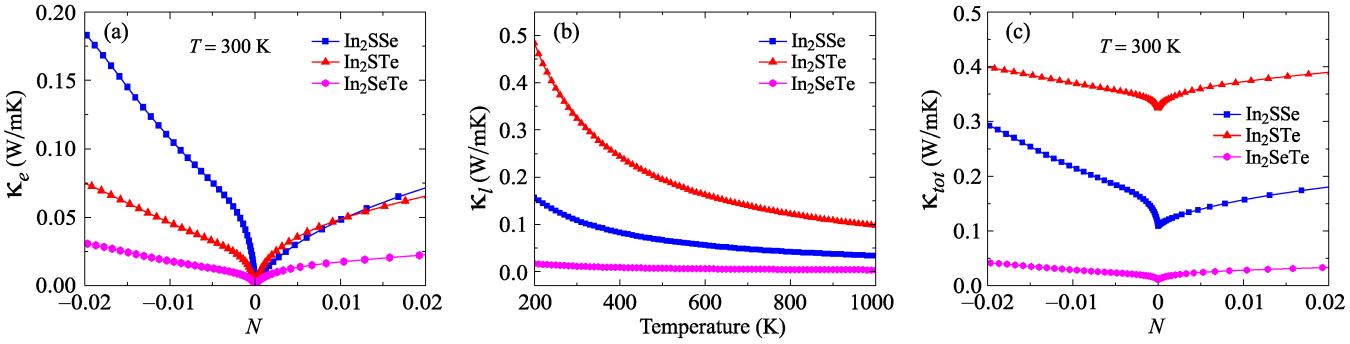


Figure 11. (a) Electronic thermal conductivity κ_e vs doping level N at 300 K, (b) lattice thermal conductivity κ_l as a function of temperature, and (c) dependence of the total thermal conductivity $\kappa_{\text{tot}} = \kappa_e + \kappa_l$ on doping level N of In_2XY .

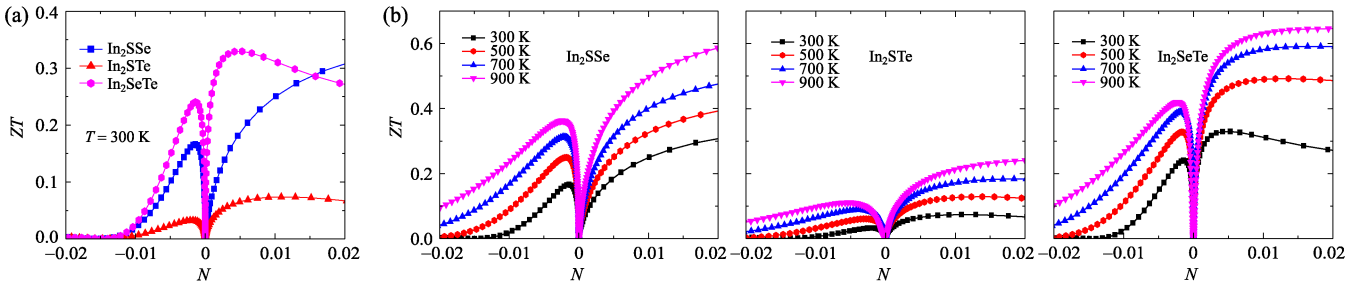


Figure 12. Doping level N dependence of figure of merit ZT of In_2XY monolayers at room temperature (a) and different values of temperature (b).

HfSSe (1.78 W mK^{-1}) [22]. The obtained low thermal conductivity on In_2XY monolayers may be due to strong acoustic-optical scattering as evident from figures 1(b)–(d). With low κ_l , In_2XY monolayers are well suited for applications in thermoelectric devices. In figure 11(b), we have presented the temperature-dependent κ_l of In_2XY monolayers. We can see that the κ_l of all three Janus structures In_2XY decreases with the temperature increasing. This is because at high temperatures there will be more phonon Umklapp scatterings. The dependence of the total thermal conductivity $\kappa_{\text{tot}} = \kappa_e + \kappa_l$ of In_2XY at 300 K on N is presented in figure 11(c). On the assumption that κ_l is independent of N , the shape of κ_{tot} is similar to that of κ_e . Similar to the κ_l , In_2STe has higher κ_{tot} than that of In_2SSe and In_2SeTe . For In_2SSe , the difference in κ_{tot} between n -type and p -type is clear, namely that the κ_{tot} for n -type is

higher than that in p -type. The lower κ_{tot} , the higher figure of merit ZT .

The doping level dependence of the thermoelectric figure of merit ZT of In_2XY monolayers is depicted in figure 12. Our calculations demonstrate that the maximum values of ZT for the p -type are higher than those for the n -type. Focusing on the ZT at 300 K as shown in figure 12(a), we can see that the maximum value of ZT of In_2SeTe for p -type is 0.330 at $N = 0.005$, compared to 0.241 at $N = 0.001$ for n -type. For p -type, the maximum ZT for In_2SeTe is at small value of N , while the ZT of In_2SSe and In_2STe is maximum at the higher value of doping level N , at $N = 0.056$ (not shown) and $N = 0.110$, respectively. For n -type, the maximum ZT for In_2SeTe is much higher than that for In_2STe (only 0.033). However, the ZT of all three structures In_2XY rapidly decreased as the concentration of electrons continued to

increase in n -type. With high ZT value, the Janus structures, such as In_2SeTe or In_2SSe , can be used effectively in thermoelectric devices. The N -dependent ZT of In_2XY monolayers is presented in figure 12(b). Obviously, the lattice thermal conductivity of the systems decreases with increasing temperature as shown in figure 11(b). Consequently, the ZT of In_2XY monolayers is higher in the higher temperature domain.

7. Conclusion

In conclusion, the structural, electronic, optical, and thermoelectric properties of the Janus monolayers In_2XY ($X/Y = \text{S}, \text{Se}, \text{Te}; X \neq Y$) have systematically been investigated by DFT study. All three Janus structures In_2XY were confirmed to be dynamically and thermally stable. The Janus In_2XY monolayers have a moderate band gap and we can alter their band gap by strain engineering. Besides, the indirect–direct band gap transitions have been found in the Janus In_2XY monolayers at certain values of ε_b and even E has led to the indirect–direct band gap transition in the In_2SeTe monolayer (at $E = -5 \text{ V nm}^{-1}$). The influence of the ε_b and E on the physical properties of the Janus In_2XY monolayers has also been investigated comprehensively. Our findings revealed that the Janus In_2XY monolayers have suitable band edge alignment for water splitting and the photocatalytic activity of Janus In_2SSe monolayer can be increased by strain engineering. The optical absorbance spectra of the Janus monolayers In_2XY are activated in the visible light region and they have high intensity in the near-ultraviolet region. The In_2XY monolayers exhibit very low lattice thermal conductivities and a high thermoelectric figure of merit ZT . With high ZT at room temperature, up to 0.330 for In_2SeTe , In_2XY monolayers have a great prospect for becoming a room temperature thermoelectric materials. Our results demonstrated that Janus monolayers In_2XY have great potential for applications in photocatalytic, optoelectronic, and high-performance thermoelectric conversion devices, which provide a strong incentive for experimental studies on the Janus structures in the future.








Acknowledgments

Vo T T Vi was funded by Vingroup Joint Stock Company and supported by the Domestic Master/PhD Scholarship Programme of Vingroup Innovation Foundation (VINIF), Vingroup Big Data Institute (VINBIGDATA), code VINIF.2020.TS.100. NA Poklonski was funded by the Belarusian National Research Program ‘Convergence-2025’. C.A. Duque acknowledges the financial support from El Patrimonio Autónomo Fondo Nacional de Financiamiento para la Ciencia, la Tecnología y la Innovación Francisco José de Caldas (project: CD 111580863338, CT FP80740-173-2019).

Data availability statement

The data that support the findings of this study are available upon reasonable request from the authors.

ORCID iDs

Tuan V Vu  <https://orcid.org/0000-0003-3872-8323>
 Chuong V Nguyen  <https://orcid.org/0000-0003-4109-7630>
 N A Poklonski  <https://orcid.org/0000-0002-0799-6950>
 C A Duque  <https://orcid.org/0000-0003-3382-2783>
 D P Rai  <https://orcid.org/0000-0002-3803-8923>
 Bui D Hoi  <https://orcid.org/0000-0002-5174-841X>
 Nguyen N Hieu  <https://orcid.org/0000-0001-5721-960X>

References

- [1] Novoselov K S, Geim A K, Morozov S V, Jiang D, Zhang Y, Dubonos S V, Grigorieva I V and Firsov A A 2004 *Science* **306** 666
- [2] Siahlo A I, Poklonski N A, Lebedev A V, Lebedeva I V, Popov A M, Vyrko S A, Knizhnik A A and Lozovik Y E 2018 *Phys. Rev. Mater.* **2** 036001
- [3] Poklonski N A, Vyrko S A, Siahlo A I, Poklonskaya O N, Ratkevich S V, Hieu N N and Kocherzhenko A A 2019 *Mater. Res. Express* **6** 042002
- [4] Siahlo A I, Popov A M, Poklonski N A, Lozovik Y E and Vyrko S A 2020 *Phys. E* **115** 113645
- [5] Vogt P, De Padova P, Quaresima C, Avila J, Frantzeskakis E, Asensio M C, Resta A, Ealet B and Le Lay G 2012 *Phys. Rev. Lett.* **108** 155501
- [6] Acun A *et al* 2015 *J. Phys.: Condens. Matter* **27** 443002
- [7] Kong D, Wang H, Cha J J, Pasta M, Koski K J, Yao J and Cui Y 2013 *Nano Lett.* **13** 1341–7
- [8] Hu X, Ding Y, Hu X, Zhou W, Yu X and Zhang S 2019 *Nanotechnology* **30** 252001
- [9] Muoi D, Hieu N N, Nguyen C V, Hoi B D, Nguyen H V, Hien N D, Poklonski N A, Kubakaddi S S and Phuc H V 2020 *Phys. Rev. B* **101** 205408
- [10] Pham K D, Hieu N N, Phuc H V, Fedorov I A, Duque C A, Amin B and Nguyen C V 2018 *Appl. Phys. Lett.* **113** 171605
- [11] Shih P-H, Do T-N, Huang B-L, Gumbs G, Huang D and Lin M-F 2019 *Carbon* **144** 608–14
- [12] Hien N D, Nguyen C V, Hieu N N, Kubakaddi S S, Duque C A, Mora-Ramos M E, Dinh L, Bich T N and Phuc H V 2020 *Phys. Rev. B* **101** 045424
- [13] Do T N, Gumbs G, Shih P H, Huang D, Chiu C W, Chen C Y and Lin M F 2019 *Sci. Rep.* **9** 624
- [14] Nguyen C V, Hieu N N, Poklonski N A, Ilyasov V V, Dinh L, Phong T C, Tung L V and Phuc H V 2017 *Phys. Rev. B* **96** 125411
- [15] Vu T V *et al* 2019 *Phys. Chem. Chem. Phys.* **21** 22140–8
- [16] Hu P, Wen Z, Wang L, Tan P and Xiao K 2012 *ACS Nano* **6** 5988–94
- [17] Hu P *et al* 2013 *Nano Lett.* **13** 1649–54
- [18] Acharya S, Dutta M, Sarkar S, Basak D, Chakraborty S and Pradhan N 2012 *Chem. Mater.* **24** 1779–85
- [19] Mudd G W *et al* 2013 *Adv. Mater.* **25** 5714–8
- [20] Demirci S, Avazli N, Durgun E and Cahangirov S 2017 *Phys. Rev. B* **95** 115409
- [21] Cui Y, Peng L, Sun L, Qian Q and Huang Y 2018 *J. Mater. Chem. A* **6** 22768–77
- [22] Dimple, Mohanta M K, Rawat A, Jena N, Ahammed R and De Sarkar A 2020 *J. Phys.: Condens. Matter* **32** 315301
- [23] Zhang J-W, Wu Z-W, Xiang B, Zhou N-N, Shi J-L and Zhang J-X 2020 *ACS Appl. Mater. Interfaces* **12** 21863
- [24] Lu A-Y *et al* 2017 *Nat. Nanotechnol.* **12** 744
- [25] Zhang J *et al* 2017 *ACS Nano* **11** 8192–8
- [26] Guo S-D and Dong J 2018 *Semicond. Sci. Technol.* **33** 085003

- [27] Din H U, Idrees M, Albar A, Shafiq M, Ahmad I, Nguyen C V and Amin B 2019 *Phys. Rev. B* **100** 165425
- [28] Yuan J, Shan Y and Li T 2020 *J. Phys. D: Appl. Phys.* **53** 125502
- [29] Sun Y, Shuai Z and Wang D 2018 *Nanoscale* **10** 21629
- [30] Yang X, Singh D, Xu Z, Wang Z and Ahuja R 2019 *J. Mater. Chem. C* **7** 12312–20
- [31] Yang H, Zhao P, Ma Y, Lv X, Huang B and Dai Y 2019 *J. Phys. D: Appl. Phys.* **52** 455303
- [32] Huang A, Shi W and Wang Z 2019 *J. Phys. Chem C* **123** 11388
- [33] Wan W, Zhao S, Ge Y and Liu Y 2019 *J. Phys.: Condens. Matter* **31** 435501
- [34] Guo Y, Zhou S, Bai Y and Zhao J 2017 *Appl. Phys. Lett.* **110** 163102
- [35] Kandemir A and Sahin H 2018 *Phys. Rev. B* **97** 155410
- [36] Giannozzi P et al 2009 *J. Phys.: Condens. Matter* **21** 395502
- [37] Perdew J P, Burke K and Ernzerhof M 1996 *Phys. Rev. Lett.* **77** 3865
- [38] MacDonald A H, Pickett W E and Koelling D D 1980 *J. Phys. C: Solid State Phys.* **13** 2675
- [39] Heyd J, Scuseria G E and Ernzerhof M 2003 *J. Chem. Phys.* **118** 8207
- [40] Nosé S 1984 *J. Chem. Phys.* **81** 511
- [41] Madsen G K H and Singh D J 2006 *Comput. Phys. Commun.* **175** 67
- [42] Togo A, Chaput L and Tanaka I 2015 *Phys. Rev. B* **91** 094306
- [43] da Silva R, Barbosa R, Mançano R R, Durães N, Pontes R B, Miwa R H, Fazzio A and Padilha J E 2019 *ACS Appl. Nano Mater.* **2** 890
- [44] Guo S-D, Guo X-S, Han R-Y and Deng Y 2019 *Phys. Chem. Chem. Phys.* **21** 24620
- [45] Guo S-D, Guo X-S and Deng Y 2019 *J. Appl. Phys.* **126** 154301
- [46] Cheng Y C, Zhu Z Y, Tahir M and Schwingenschlögl U 2013 *Europhys. Lett.* **102** 57001
- [47] Yao Q F, Cai J, Tong W Y, Gong S J, Wang J Q, Wan X, Duan C G and Chu J H 2017 *Phys. Rev. B* **95** 165401
- [48] Perdew J P and Levy M 1983 *Phys. Rev. Lett.* **51** 1884–7
- [49] Hedin L 1965 *Phys. Rev.* **139** A796
- [50] Chakrapani V, Angus J C, Anderson A B, Wolter S D, Stoner B R and Sumanasekera G U 2007 *Science* **318** 1424
- [51] Pham T A, Lee D, Schwegler E and Galli G 2014 *J. Am. Chem. Soc.* **136** 17071–7
- [52] Liu J J, Fu X L, Chen S F and Zhu Y F 2011 *Appl. Phys. Lett.* **99** 191903
- [53] Delin A, Ravindran P, Eriksson O and Wills J M 1998 *Int. J. Quant. Chem.* **69** 349
- [54] Karazhanov S Z, Ravindran P, Kjekshus A, Fjellvåg H and Svensson B G 2007 *Phys. Rev. B* **75** 155104
- [55] Ravindran P, Delin A, Johansson B, Eriksson O and Wills J M 1999 *Phys. Rev. B* **59** 1776–85
- [56] Hicks L D and Dresselhaus M S 1993 *Phys. Rev. B* **47** 16631
- [57] Pei Y, Shi X, LaLonde A, Wang H, Chen L and Snyder G J 2011 *Nature* **473** 66
- [58] Yu D, Zhang Y and Liu F 2008 *Phys. Rev. B* **78** 245204
- [59] Jin Z, Liao Q, Fang H, Liu Z, Liu W, Ding Z, Luo T and Yang N 2015 *Sci. Rep.* **5** 18342
- [60] Bardeen J and Shockley W 1950 *Phys. Rev.* **80** 72–80
- [61] Bruzzone S and Fiori G 2011 *Appl. Phys. Lett.* **99** 222108
- [62] Kaasbjerg K, Thygesen K S and Jacobsen K W 2012 *Phys. Rev. B* **85** 115317
- [63] Rai D P, Vu T V, Laref A, Hossain M A, Haque E, Ahmad S, Khenata R and Thapa R K 2020 *RSC Adv.* **10** 18830–40
- [64] Vu T V et al 2021 *Phys. Rev. B* **103** 085422
- [65] Tan Q, Zhao L-D, Li J-F, Wu C-F, Wei T-R, Xing Z-B and Kanatzidis M G 2014 *J. Mater. Chem. A* **2** 17302
- [66] Ding G, He J, Cheng Z, Wang X and Li S 2018 *J. Mater. Chem. C* **6** 13269–74